Journal of The Electrochemical Society, **153** (11) C777-C786 (2006)
0013-4651/2006/153(11)/C777/10/$20.00 © The Electrochemical Society

Characteristics of Polycrystalline $SrRuO_3$ Thin-Film Bottom Electrodes for Metallorganic Chemical-Vapor-Deposited $Pb(Zr_{0.2}Ti_{0.8})O_3$ Thin Films

Joon Seop Sim, Jin Shi Zhao, Hyun Ju Lee, Keun Lee, Gyu Weon Hwang, and Cheol Seong Hwang*,z

School of Materials Science and Engineering, and Inter-university Semiconductor Research Center, Seoul National University, Kwanak-ku, Seoul 151-742, Korea

In situ and ex situ crystallized polycrystalline $SrRuO_3$ (SRO) thin-film electrodes are fabricated by dc magnetron sputtering at a substrate temperature of 550 and 350°C, respectively, followed by postannealing for application as bottom electrodes of metal-lorganic chemical-vapor-deposited $Pb(Zr_{0.2}Ti_{0.8})O_3$ (PZT) thin films. The in situ crystallized SRO electrode shows a negligible change in film composition during the subsequent annealing and works as a good electrode for the ferroelectric PZT films. However, the ex situ crystallization by postannealing largely decreases the Ru content in the SRO film and consequently the PZT film grown on top has a poor ferroelectric performance. In addition, the Zr component in the PZT film initially reacts with the excessive SrO in the electrode, resulting in a deposition of $PbTiO_3$ at the initial stage of the PZT deposition which largely deteriorates the ferroelectric performance. Therefore, it is crucial to have in situ crystallized SRO for a reliable electrode of a PZT capacitor.
 [DOI: 10.1149/1.2344839]

Manuscript submitted March 20, 2006; revised manuscript received June 12, 2006. Available electronically September 12, 2006.

Confirming the long-term reliability of ferroelectric $Pb(Zr,Ti)O_3$ (PZT) thin film capacitors, including fatigue (loss of the ferroelectric switching property by repeated polarization switching) and opposite state retention (OSR) loss (switching back of one polarization state to the opposite state after a long stay at the opposite polarization state), has been one of the major issues for their application to ferroelectric random access memories (FeRAM).[1] Although metal-lorganic chemical vapor deposition (MOCVD) of PZT thin films has reduced the problems compared to other techniques, such as sol-gel or sputtering,[2] further improvements are required as the FeRAM integration density increases. One effective method to improve the reliability challenges is the adoption of conducting oxide electrodes, such as IrO_2 [3] and $SrRuO_3$ (SRO),[4] which is effective in suppressing the defect generation (probably oxygen vacancies) and migration. Among the various conducting oxide electrodes, the SRO electrode recently attracts large attention due to its structural compatibility (pseudocubic perovskite structure) with PZT and therefore an eventual improvement of the ferroelectric performance of PZT capacitors.

In conjunction with the epitaxial ferroelectric layers on top, epitaxial SRO electrodes fabricated on $SrTiO_3$ single crystals have been extensively studied during the past decade.[5-7] Although these epitaxial systems have served as good model systems to understand the fundamental properties of ferroelectric thin-film capacitors, such as the ultimate thickness for ferroelectricity[6] and strain effects on the ferroelectric properties,[5] these systems are of limited application to FeRAM integration due to a missing technique for an integration in the Si-based device structure. All the reported highly integrated devices have polycrystalline ferroelectric capacitors based on the capacitor-under-bit-line or capacitor-on-bit-line structure. Therefore, the structural investigation of a polycrystalline SRO (poly-SRO) electrode and its interaction with the MOCVD PZT film grown on top are of crucial importance when considering the FeRAM application.

Two fabrication processes for poly-SRO electrodes are possible: in situ crystallization by adopting a high growth temperature (>500°C) and ex situ crystallization by adopting a low growth temperature (<400°C) during the SRO film deposition followed by high-temperature postdeposition annealing (PDA) at temperatures >600°C. Sputtering of an SRO electrode at such a high temperature (>500°C) on large wafers (>8 in. diam.) is a rather difficult process and requires high production costs. Therefore, a low growth temperature is preferred when considering mass production of FeRAM devices.

Aggarwal et al. reported the variations in the ferroelectric performance of sol-gel derived $Pb(Nb,Zr,Ti)O_3$ thin films on poly-SRO electrodes depending on the growth temperature of the poly-SRO electrode (550–850°C).[8] Aoki et al. also reported the crystallization and ferroelectric behaviors of sol-gel-derived PZT thin films on a sputtered in situ crystallized poly-SRO electrode which was grown at 600°C.[9] Cross et al. reported the crystallization and ferroelectric behaviors of sol-gel-derived PZT thin films on ex situ and in situ crystallized poly-SRO electrodes fabricated by sputtering on Pt electrodes at room temperature followed by annealing at 600°C and 600°C, respectively.[10] They reported that the in situ crystallized poly-SRO electrode was more beneficial in obtaining better ferroelectric performances, as in the present report. However, they did not show the detailed characterization results on the ex situ crystallized SRO films, such as the film composition variation and their influence on the PZT film properties. In addition, the results in Ref. 8 and 9 are from the sol-gel-derived PZT films which have a limited usefulness in high-density FeRAMs. More relevant data must be found from MOCVD films. A research group at Tokyo Institute of Technology has reported many experimental results on the MOCVD PZT/SRO and SRO itself with epitaxial and polycrystalline film structures. Some of them are included in Ref. 11. For the MOCVD SRO case, the in situ crystallization was also crucial in obtaining reliable ferroelectric PZT thin films.[11]

In this paper, the structural and electrical properties of in situ and ex situ poly-SRO films grown by dc magnetron sputtering are investigated and their influence on the crystallization and ferroelectric performance of MOCVD PZT films grown at 550°C is systematically studied. For that purpose, three types of substrates were used for the SRO film deposition: 10 nm thick Ta_2O_5/Si (type I), 100 nm thick Ir/50 nm thick IrO_2/100 nm thick SiO_2/Si (type II), and 20 nm thick Ru/100 nm thick SiO_2/Si (type III) substrates. The Ta_2O_5 film was grown by MOCVD and the Ru, Ir, and IrO_2 films were deposited by sputtering. Type I substrates were used to investigate the basic deposition properties and changes during PDA of the SRO films. Type I substrate was also used for checking the variation in electrical property of the SRO layer as a function of postannealing temperature and atmosphere. In integrated capacitor structures using Ru electrodes Ta_2O_5 layer works as a good adhesion and nucleation-enhancing layer.[12] Therefore, testing the SRO layer on top of the Ta_2O_5 layer is important under the assumption that the SRO layer replaces Ru electrodes in integrated device.

* Electrochemical Society Active Member.
z E-mail: cheolsh@snu.ac.kr

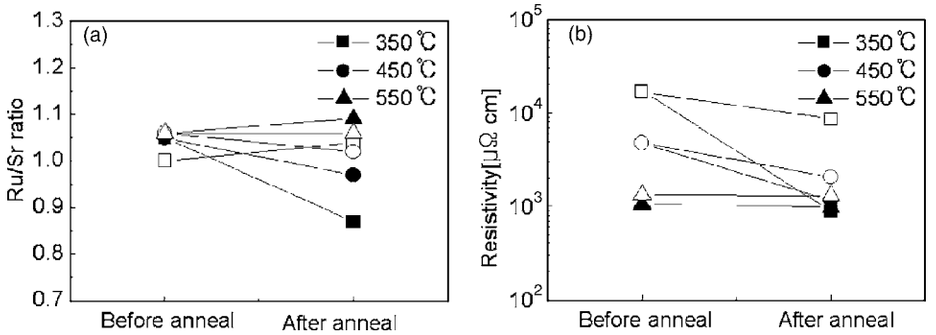

Figure 1. Variations in the (a) cation composition ratio (Ru/Sr) and (b) resistivity of the SRO films grown on a type I substrate before and after PDA at 600°C for 1 min in O_2 (closed symbol) or N_2 (open symbol) atmosphere.

Type III served as the major substrate for PZT film capacitor fabrication. As shown later, the in situ crystallized poly-SRO electrode was chemically stable and showed almost no change during the subsequent processes. The amorphous SRO electrode (or ex situ crystallized poly-SRO electrode) was chemically unstable and its chemical composition changed with the PDA temperature and condition as shown below. Therefore, it was necessary to check the SRO film cation composition during processing, which precludes the Ru bottom layer because the Ru layer adversely interferes with the routine cation composition measurements using X-ray fluorescence spectroscopy (XRF). Ir was selected as the bottom layer for the ex situ poly-SRO film growth (type II substrate). An IrO_2 layer improved the adhesion between Ir and SiO_2. In addition to that reason, it was considered that the crystallization behavior of the amorphous SRO film may depend on the crystal structure of the underlying layer. Therefore, an Ir layer was adopted because this is the most commonly adopted bottom electrode layer for the MOCVD of PZT films in integrated FeRAM devices.[13-16] SRO has a too high resistivity to be used as a bottom electrode of highly integrated FeRAMs. For the fabrication of FeRAMs with a higher density (>32 Mbit) a lower height of the capacitor stack is necessary due to the difficult etching of the stack with a vertical side wall shape.[14] Therefore, a lower electrode thickness is necessary, but SRO single layers can hardly be used due to the high resistivity (bulk resistivity of ~110 μΩ cm).[17] A metal electrode, such as Ir or Ru, is still preferred as main electrode and the thin SRO layer works as buffer layer.[4] Therefore, the investigation of the crystallization behavior of amorphous SRO on an Ir electrode is of vital importance.

Experimental

SRO thin films were grown by dc magnetron sputtering using a sintered SRO ceramic target. The SRO deposition power and chamber pressure were 100 W and 30 mTorr, respectively. The SRO thickness was changed from 5 to 40 nm. SRO films (40 nm thick) were deposited on type I substrates at 350, 450, and 550°C, respectively. An in situ crystallized poly-SRO electrode was fabricated on a type III substrate by depositing the SRO films at 550°C. Ex situ poly-SRO layers were grown on type II substrates at 350°C, followed by PDA at 600°C in N_2 or O_2 atmosphere. PDA was performed using a conventional furnace or rapid thermal annealing (RTA) process. Some of the SRO layers were heat-treated under the O_3 or O_2 atmosphere considering the generally low oxygen partial pressure of the sputtering process.

On the various amorphous- and poly-SRO electrodes, PZT thin films were grown using an 8 in. scale dome-type liquid-delivery MOCVD reactor at a substrate temperature of 550°C. A schematic diagram and detailed features of the dome-type MOCVD system were reported previously.[13] Bis-tetramethylheptanedionato-Pb $[Pb(THD)_2]$, tetrakis 1-methoxy-2-methyl-2-propoxy-Zr $[Zr(MMP)_4]$, and tetrakis 1-methoxy-2-methyl-2-propoxy-Ti $[Ti(MMP)_4]$ dissolved in an ethylcyclohexane (ECH) solvent (concentration of 0.1 M) were used as Pb, Zr, and Ti precursors, respectively, and O_2 was used as an oxidant. The typical PZT film thickness was 70 nm.

The film thickness was measured by both field-emission scanning electron microscopy (FESEM) and ellipsometry, which was calibrated by cross-sectional high-resolution transmission electron microscopy (HRTEM). The cation composition of the films was measured by XRF (Spectrace, Quan-X). The error in the quantitative film composition measurement was estimated to be $< \sim 2\%$. The film surface morphology was investigated using SEM and atomic force microscopy (AFM). Auger electron spectroscopy (AES) was used to obtain depth profiles. θ–2θ mode X-ray diffraction (XRD) was used to investigate the crystalline structure. The chemical binding status of the films and the substrate surfaces were investigated by X-ray photoelectron spectroscopy (XPS). For the electrical measurements, 80 nm thick Pt electrodes with a diameter of 0.3 mm were fabricated at room temperature by electron beam evaporation through a metal shadow mask. The accurate area of each measured capacitor was obtained by optical microscopy. The top electrodes were annealed in ambient atmosphere at 600°C for 30 min. An aixACCT TF-2000 analyzer at a frequency of 100 Hz was used to measure the ferroelectric parameters. During the ferroelectric hysteresis measurements, the bias voltage was applied to the top electrode.

Results and Discussion

Variations in the SRO electrode properties with growth temperature.— Figure 1a and b shows the variations in the cation composition ratio (Ru/Sr) and resistivity, respectively, of SRO films grown on type I substrates before and after PDA at 600°C for 1 min in O_2 or N_2 atmosphere. Here, the SRO films were grown at a growth temperature (T_g) of 350, 450, and 550°C, respectively. It can be observed that the Ru/Sr ratio of the as-grown films is ~1.05 irrespective of T_g. However, the resistivity of the as-grown film drastically increases with decreasing T_g (~1 mΩ cm at 550°C and ~20 mΩ cm at 350°C) which is due to the amorphous-like nature of the SRO film grown at a lower T_g. The estimated resistivity of the SRO film is higher than that of bulk SRO (~110 μΩ cm)[17] even for the film grown at the highest temperature. Okuda et al. reported that the resistivityof the SRO film grown by MOCVD at 750°C on single crystalline $LaAlO_3$ substrate was ~280 μΩ cm.[11] The polycrystalline nature and small grain size of the SRO film in the present experiment may have resulted in high resistivity. In order to improve the crystallinity of the as-grown films, and thus decrease the resistivity, the SRO films were PDA-treated. The Ru/Sr ratio of the films shows large variations depending on T_g and the PDA atmosphere. When T_g is low (350°C) and the PDA atmosphere is oxygen, the Ru/Sr ratio largely decreases, whereas the SRO film grown at 550°C shows a negligible change. The reduction in the Ru concentration of the films grown at a lower T_g is attributed to the formation of volatile RuO_3 or RuO_4 during

PDA in O_2 atmosphere.[18] The nonvarying Ru/Sr ratio of the film grown at 550°C suggests that the formation of RuO_3 or RuO_4 by the reaction of crystallized SRO with O_2 is not probable. Conversely, the constituent elements in the amorphous as-deposited films loosely bound with each other. During the PDA of the amorphous SRO film, the crystallization and reaction with O_2 forming the volatile components simultaneously occur, as shown by XRD later. The remaining SrO is amorphous or nanocrystalline as no XRD peak corresponding to SrO is detected. However, it is interesting to note that the resistivities of the three films grown at three different T_g after PDA in O_2 atmosphere are almost identical, as shown in Fig. 1b. The resistivity of the SRO film grown at 550°C shows a negligible change, while that of the film grown at a lower T_g shows a large decrease. This suggests that the in situ crystallized film (grown at a T_g of 550°C) experiences almost no change in structure and cation composition during PDA in O_2 atmosphere. However, the amorphous as-deposited film undergoes a rather serious structural and cation composition change during PDA. However, the almost identical resistivity of the SRO film grown at 350°C after PDA in O_2 atmosphere to that of the in situ crystallized film suggests that the crystallized SRO parts are rather large, so that they percolate to form fluent electrical conduction paths. However, as shown in the next section, these ex situ crystallized poly-SRO films are not proper as the electrode for the ferroelectric PZT film deposition.

PDA in N_2 atmosphere induced a negligible change in the cation composition of the SRO films irrespective of T_g. This supports the hypothesis that the reduction in the Ru content during PDA in O_2 atmosphere is due to the formation of volatile RuO_3 or RuO_4. Unfortunately, PDA in N_2 atmosphere does not lead to crystallization (see Fig. 3) of the amorphous as-deposited SRO films. Accordingly, the resistivity of the SRO film grown at 350°C still remains at a higher value (Fig. 1b). The resistivity of the in situ crystallized SRO film shows a negligible change by PDA in N_2 atmosphere too.

Figure 2a shows the SEM surface morphology of the SRO films grown at a T_g of 350, 450, and 550°C, respectively, and b and c show the surface morphologies after PDA in O_2 and N_2 atmosphere, respectively. As T_g increases, the size of clusters (for an amorphous layer) or grains (for a crystalline layer) of the as-deposited SRO films increases. PDA in O_2 atmosphere largely increases the average grain size of the SRO film grown at a lower T_g, but almost no change is observed for the film grown at 550°C. The root-mean-squared (rms) roughness measured by AFM is $\sim$0.5 and $\sim$4 nm, respectively, for the as-grown film grown at 350°C and after PDA. Along with the roughening of the SRO film grown at a lower T_g, many small pores are formed mainly at the grain boundaries, which might be closely related to the loss of Ru. When the PDA atmosphere was changed to N_2, a negligible change in the cluster or grain structure is observed. XRD analysis was performed to investigate the variations in the crystal structure of the SRO film grown at 350°C with PDA temperature. Here, the SRO film was grown on type II substrates with different thicknesses of 5, 20, and 40 nm. The reason for adopting type II substrates has been explained above.

Figure 3a and b shows the XRD patterns of 5, 20, and 40 nm thick SRO/type II substrate samples after PDA using a conventional furnace for 30 min at 600°C in O_2 and N_2 atmosphere, respectively. In addition to the XRD peaks from the type II substrate (Ir and IrO_2) a (110) peak corresponding to pseudocubic SRO is observed for a thicker film ($>$20 nm) when PDA was performed in O_2 atmosphere. When N_2 atmosphere was used during PDA, no peak corresponding to SRO was observed. Figure 3c shows the XRD patterns of an as-deposited 40 nm thick SRO film grown on a type III substrate at a T_g of 550 and 350°C, respectively. The SRO film grown on a type III substrate at 350°C is also amorphous, whereas the film grown at 550°C is in situ crystallized with a pseudocubic 110-preferred growth direction.

Figure 4a and b shows the variations in the Ru/Sr composition ratio of the 5, 20, and 40 nm thick SRO/type II substrate samples after PDA at 600°C by RTA and furnace, respectively. For the PDA

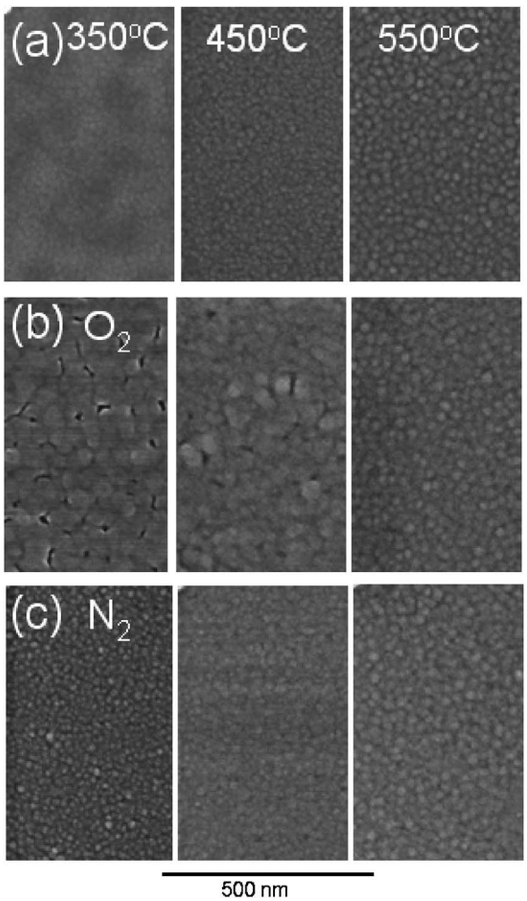

Figure 2. SEM surface morphology of SRO films grown at a T_g of 350, 450, and 550°C (a) at the as-deposited state, and after the PDA at 600°C under the (b) O_2 and (c) N_2 atmospheres.

using RTA the atmosphere was O_2, and for the PDA using the furnace the atmosphere was O_2 or N_2. The initial Ru/Sr ratio of the films was measured to be slightly higher ($\sim$1.1) than that on type I substrates ($\sim$1.05). However, the trends in variation of the Ru/Sr ratio of the film with PDA were almost identical to that on type I substrates shown in Fig. 1. As the SRO thickness becomes smaller, the relative variation becomes large due to the relatively larger portion of surface layer where the loss of Ru is more serious. For the case of PDA in O_2 atmosphere using a furnace, the variation with the annealing time saturates depending on the SRO thickness, which suggests that the Ru loss from the film becomes less active as the film crystallizes. Figure 4c shows the variation in rms surface roughness of the 5, 20, and 40 nm thick SRO/type II substrate samples measured by AFM under various PDA conditions. The roughness generally increases with increasing Ru loss and degree of crystallization.

Figure 5 shows the AES depth profile results of the 40 nm thick SRO/type II substrate sample grown at 350°C (a) at the as-deposited state and after RTA at 600°C in (b) O_2 and (c) N_2 atmosphere. For an easy comparison, only the Ru profiles are collected in Fig. 5d. It can be confirmed that PDA induces the Ru loss, especially in O_2 atmosphere. The Ru loss is most serious near the film surface, but the film bulk also looses Ru.

Figure 6a and b shows the Sr 3d XPS spectra of the amorphous (T_g of 350°C) and crystalline (T_g of 550°C) SRO films, respectively. The Sr 3d peak of the in situ crystallized SRO film can be deconvoluted with two components centered at binding energies (BE) of 132.1 and 132.9 eV, which may correspond to pseudocubic $SrRuO_3$

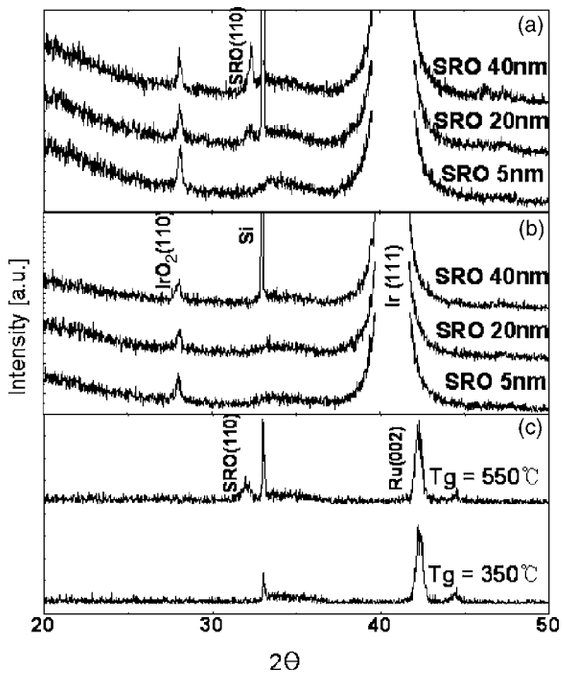

Figure 3. XRD patterns of 5, 20, and 40 nm thick SRO/type II substrate samples after PDA using a conventional furnace for 30 min at 600°C in (a) O_2 and (b) N_2 atmosphere, and (c) XRD patterns of an as-deposited 40 nm thick SRO film grown on a type III substrate at a T_g of 550 and 350°C.

and $SrRu_2O_4$, respectively.[19] However, the Sr 3d peak of amorphous SRO seems to be composed of two BE components located near a BE of 133.0, which might be related to amorphous SRO, and 134.2 eV, which is close to the BE of metallic Sr.

Therefore, it can be understood that amorphous SRO has a less-stable chemical binding status compared to in situ crystallized SRO. This results in an unstable PZT MOCVD behavior, as shown later.

Growth and ferroelectric properties of PZT films on amorphous or ex situ poly-SRO electrodes (type II substrates).— PZT thin films were grown on SRO/type II substrates. The SRO film was grown at a T_g of 350°C. Figure 7a and b shows the variations in the Pb/(Zr + Ti) (Pb ratio) and Zr/(Zr + Ti) (Zr ratio) concentration ratio (measured by XRF) of a ~15 nm thick PZT film as a function of the precursor input ratio [PIR, $Pb_{pf}/(Zr + Ti)_{pf}$, where Pb_{pf} and $(Zr + Ti)_{pf}$ are the Pb and (Zr + Ti) solution precursor flow rates, respectively], grown on as-deposited SRO electrode. The Pb and Zr ratios of the same films grown on Pt and Ir electrodes are also shown in Fig. 7.

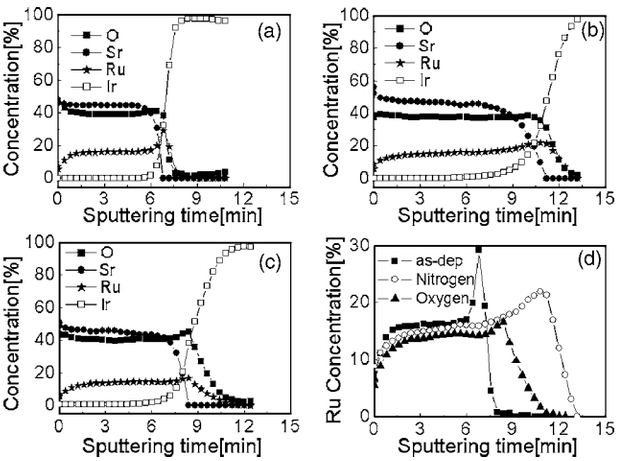

Figure 5. AES depth profile of a 40 nm thick SRO/type II substrate sample grown at 350°C (a) at the as-deposited state and after RTA at 600°C in (b) O_2 and (c) N_2 atmosphere.

Although MOCVD of multicomponent oxide thin films is quite complicated in general, MOCVD of PZT at a high enough deposition temperature (>550°C) has a crucial merit in film cation composition control to the stoichiometric value (Pb/(Zr + Ti) ~ 1) due to the presence of self-regulation (SR).[20,21] Within the SR growth window, the film cation composition ratio remains stoichiometric irrespective of PIR due to the active re-evaporation of excessively adsorbed Pb and less active oxidation of Pb compared to Zr and Ti.[20,21] The SR behavior in Pb concentration is clearly observed in Fig. 7a. The reason for the slightly higher Pb ratio of the PZT films on Pt electrodes is due to the formation of a Pb_xPt_y alloy. This was reported in detail in a separate paper.[22]

The variation in the Zr ratio depending on the types of electrodes should be noted (Fig. 7b). Because the Zr and Ti precursors are mixed in a single cocktail solution, the Zr/Zr + Ti precursor input ratio (Zr_{pf}/Ti_{pf} = 0.2:0.8) cannot be changed. On the Pt and Ir electrodes, the Zr ratio of the PZT film is almost identical to the input Zr/Ti ratio but it is almost double of the other films on amorphous SRO. Therefore, it can be expected that the rather unstable nature of the amorphous SRO film may cause a selective adsorption of Zr ions during the initial stage of the PZT MOCVD.

The variations in the Zr ratio of the PZT films grown on amorphous SRO, Pt, and Ru films for two deposition times were investigated by XRF. It was found that the Zr ratio of the PZT film on amorphous SRO decreases with the increasing deposition time (0.39 at 5 min and 0.24 at 20 min), whereas that of the film on Pt and Ru is almost independent of deposition time (0.17). This result clearly

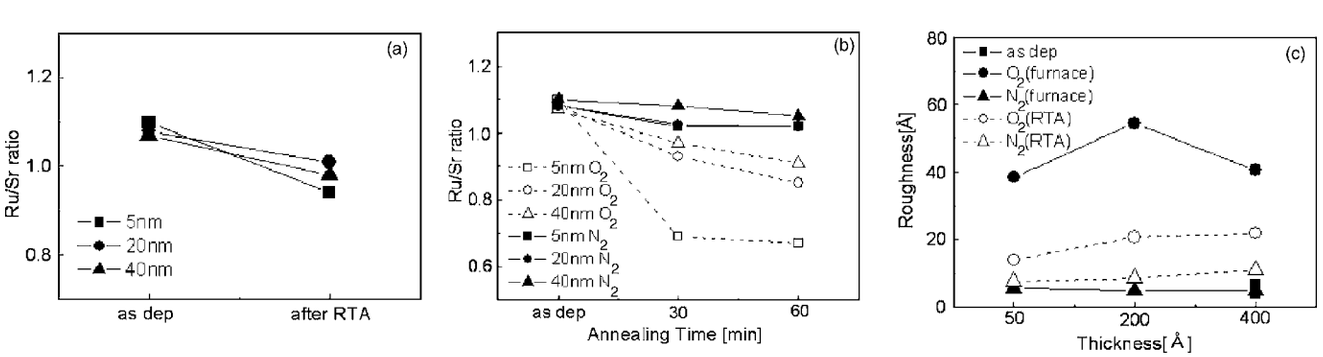

Figure 4. Variations in the Ru/Sr composition ratio of 5, 20, and 40 nm thick SRO/type II substrate samples after PDA at 600°C by RTA and furnace.

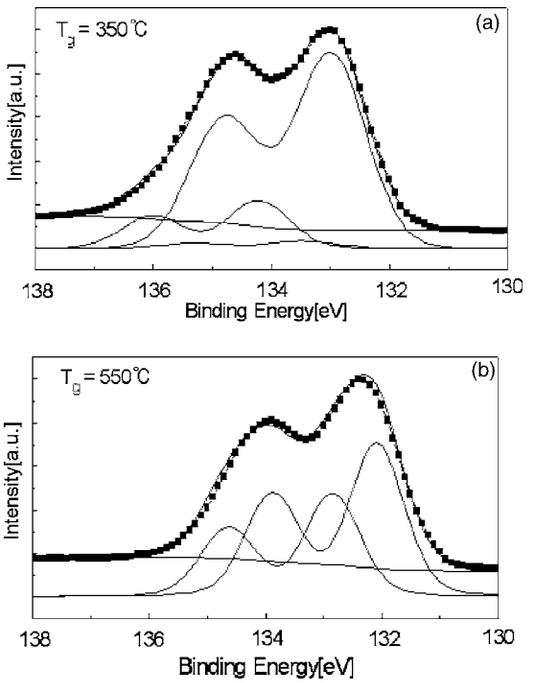

Figure 6. Sr 3d XPS spectra of (a) amorphous (T_g of 350°C) and (b) crystalline (T_g of 550°C) SRO films.

elucidates that there is a reason for the higher Zr incorporation during the initial stage of PZT MOCVD only on amorphous SRO.

In order to understand the change that happens during the PZT film growth, XPS data of the PZT films deposited for two different times grown on Pt and amorphous SRO electrodes are obtained. Figure 8a and b show the Zr 3d XPS spectra of a PZT film on Pt and amorphous SRO electrodes, respectively. The positions of the XPS peaks are calibrated using the adventitious C 1s signal. The Zr 3d XPS spectra of the PZT film on a Pt electrode shows a negligible change with deposition time, suggesting that the growth behavior was under steady state from the beginning. The Zr 3d peaks were deconvoluted assuming that there are two Zr binding states, one from the perovskite PZT structure (BE near 181.5 eV) and the other from residual ZrO_2 (BE near 182.5 eV).[23] However, the PZT film grown on the amorphous SRO film for 5 min shows quite a different Zr 3d XPS spectrum. The deconvolution reveals that most of the Zr binding status is quite different from perovskite PZT shown in Fig. 8a. The major component of the peak locates near a BE of 181.0 eV with a minor ZrO_2 component. Although the origin of the Zr 3d peak near a BE of 181.0 eV is not clearly understood, this peak might originate from the Zr ions which have reacted with Sr and O. This canbe confirmed from the following two reasons: as discussed

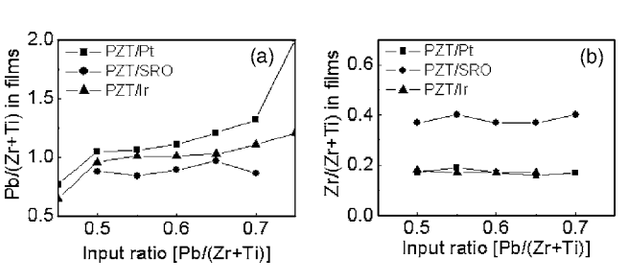

Figure 7. Variations in the (a) Pb/(Zr + Ti) and (b) Zr/(Zr + Ti) concentration ratio (measured by XRF) of ~15 nm thick PZT films as a function of the precursor input ratio, (PIR, $Pb_{pf}/(Zr + Ti)_{pf}$ on Pt, Ir, and SRO electrodes.

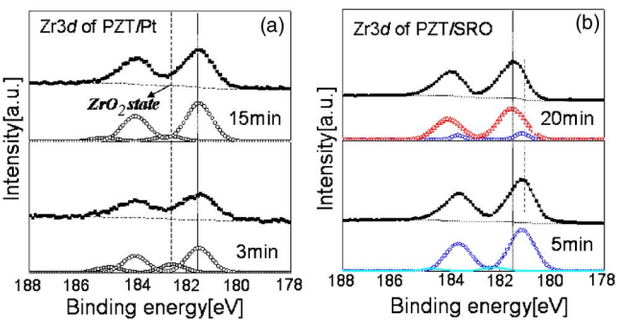

Figure 8. Zr 3d XPS spectra of a PZT film (5 and 20 min) on (a) Pt and (b) amorphous SRO electrodes.

earlier, the PZT film on a Ru electrode shows no change in the Zr ratio with the growth time, suggesting that the Zr reaction with the Ru electrode is not probable. The other reason can be found from the change in XPS of the Sr 3d peaks of the SRO electrode with PZT deposition, as shown later. In addition, Sr in the amorphous SRO has a certain metallic portion, suggesting that this layer is very vulnerable to the chemical reaction with the deposited PZT layer on top. Figure 9a and b shows the Ti 2p XPS spectra of PZT films on Pt and amorphous SRO electrodes, respectively. Although a detailed deconvolution of these peaks was not attempted, it can be observed that BE of the Ti 2p peak is almost independent of the PZT deposition time and types of electrodes. Therefore, it can be understood that the Ti component of PZT does not react with underlying layers.

Now, it can be anticipated that the growing film on top of the amorphous SRO layer is mostly constituted of $PbTiO_3$ (PT) and not PZT, because most of the Zr component from the Zr precursor reacts with the underlying Sr or SrO. This can be confirmed from the XRD analysis shown in Fig. 10, where the XRD spectra of a PZT film, grown on a 5, 20, and 40 nm thick (a) as-deposited SRO film (T_g of 350°C), and PDA-treated SRO film at 600°C for 30 min in (b) O_2 and (c) N_2 atmosphere using a furnace, are shown. Here, the PZT deposition time was 20 min, which corresponds to a nominal film thickness of 50 nm. The PZT films grown on top of the PDA-treated SRO electrodes do not show any crystalline peak due to the poor crystallization of the films on these PDA-treated SRO films irrespective of the SRO thickness and PDA atmosphere. The PZT film simultaneously grown on an Ir electrode shows a relatively good crystallization behavior with a 100- and 001-preferred growth direction (data not shown). However, the film grown on the amorphous SRO electrode shows a peak at 2θ of 39.1°, which corresponds to the PT (111) plane. As the amorphous SRO film becomes thicker, the peak intensity increases. There is no other peak corresponding to Sr–Zr–O compounds, so that these compounds have an amorphous structure. This is a reasonable result considering the easier crystallization of PT compared to PZT during MOCVD.[24] The assignment

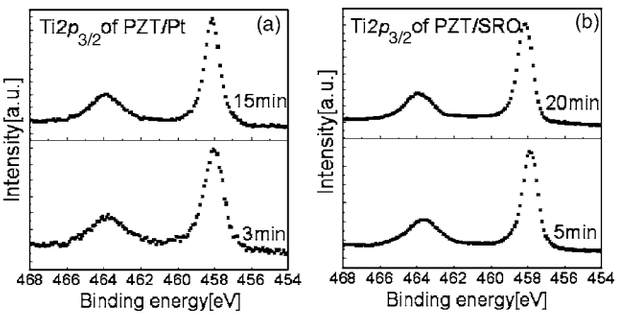

Figure 9. Ti 2p XPS spectra of a PZT film (5 and 20 min) on (a) Pt and (b) amorphous SRO electrodes.

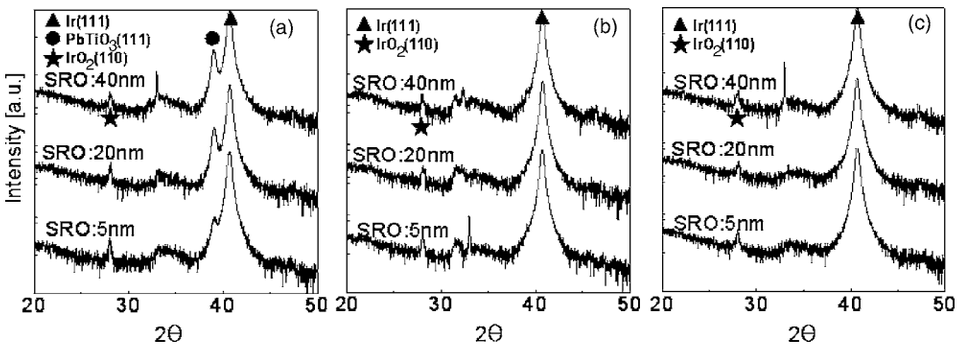

Figure 10. XRD spectra of a PZT film grown on a 5, 20, and 40 nm thick (a) as-deposited SRO film (T_g of 350°C), and PDA-treated SRO at 600°C for 30 min in (b) O_2 and (c) N_2 atmosphere using a furnace.

of the peak at 2θ of 39.1° in Fig. 10a as a PT(111) peak was further confirmed in the following way. A few PT films were grown using Ti precursor instead of the Zr + Ti cocktail solution with the same Pb solution during MOCVD at the same temperature for the same time (20 min). XRD spectra from the PT/as-deposited SRO and PZT/as-deposited SRO are almost identical (strong peak at 2θ of 39.1°), confirming that PT and not PZT is deposited on amorphous SRO. Therefore, it can be concluded that the amorphous SRO and ex situ crystallized SRO by PDA are not proper electrodes for the ferroelectric PZT film deposition by MOCVD. The XRD pattern of the PZT film deposited for 35 min is similar to that of the PZT film grown on an Ir electrode. It is interesting to note that the PT(111) peak disappears after a PZT film growth of a longer time (35 min). This suggests that the PT film serves as a seed layer for the PZT film crystallization during the later stage of PZT MOCVD and they react with the lately growing layer to form a single layer of PZT. Similar behavior has been reported earlier.[25]

Figure 11 shows the ferroelectric P–V hysteresis loops of the 70 nm thick PZT (actually PT) films grown on (a) as-deposited amorphous and (b) PDA-treated (RTA in O_2 atmosphere) 5 nm thick SRO/type II substrate samples, respectively, and (c) and (d) correspond to (a) and (b) except for a thicker SRO layer (20 nm). When the SRO thickness was 40 nm, all the PZT films were so leaky that the P–V loops could not be measured. It can be understood that the thicker amorphous SRO film made the P–V loop less stable due to the high leakage current. When the SRO thickness was as small as 5 nm, reasonable P–V loops were obtained. However, the P–V loops on the as-deposited SRO film show a slanted and nonsaturating P–V behavior. When the SRO layer was O_2-RTA-treated before the PZT MOCVD, the P–V loops improved slightly, as shown in Fig. 11d, but they are still unsatisfactory for FeRAM application. Therefore, PZT films are grown on in situ crystallized SRO electrodes as shown in the following section. Before the PZT data on the in situ crystallized SRO are discussed, the reason for the higher leakage of the PZT film on the amorphous SRO film is further studied by XPS.

Figure 12a and b shows the Pb 4f and Sr 3d spectra of the PZT film deposited for 1 min (to obtain a Sr 3d signal from the SRO layer) on amorphous SRO and in situ crystallized SRO (T_g = 550°C) electrodes, respectively. The Sr 3d spectra of these two samples were also shown in Fig. 6. Regarding the Pb 4f spectra, deconvolution shows that Pb has two oxidation states (Pb_3O_4 and PbO_2)[26] when the film is grown on amorphous SRO, whereas the

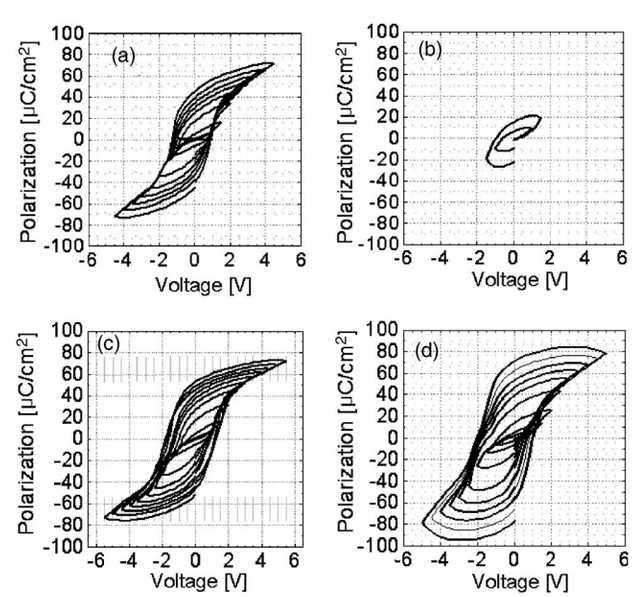

Figure 11. Ferroelectric P–V hysteresis loops of 70 nm thick PZT (actually PT) films grown on (a) an as-deposited amorphous SRO/type II substrate sample and (b) a PDA-treated 5 nm thick SRO/type II substrate sample (RTA in O_2 atmosphere); (c) and (d) correspond to (a) and (b) except for a 20 nm SRO layer.

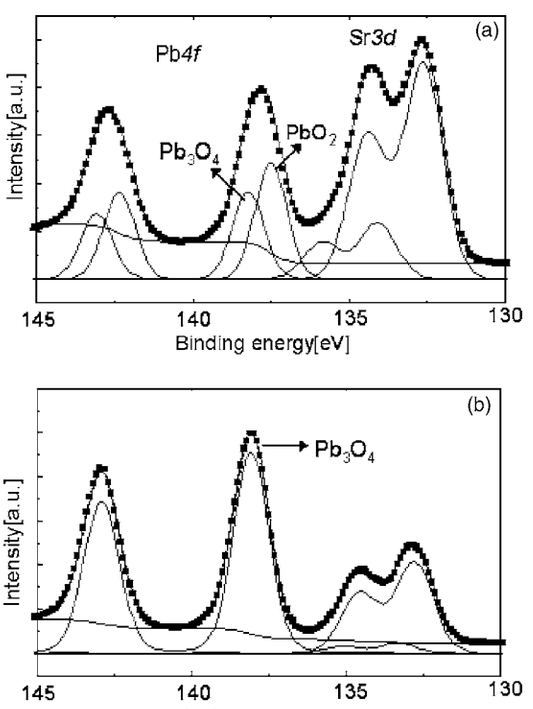

Figure 12. Pb 4f and Sr 3d XPS spectra of a PZT film deposited for 1 min (to obtain a Sr 3d signal from the SRO layer) on (a) amorphous SRO and (b) in situ crystallized SRO (T_g = 550°C) electrodes.

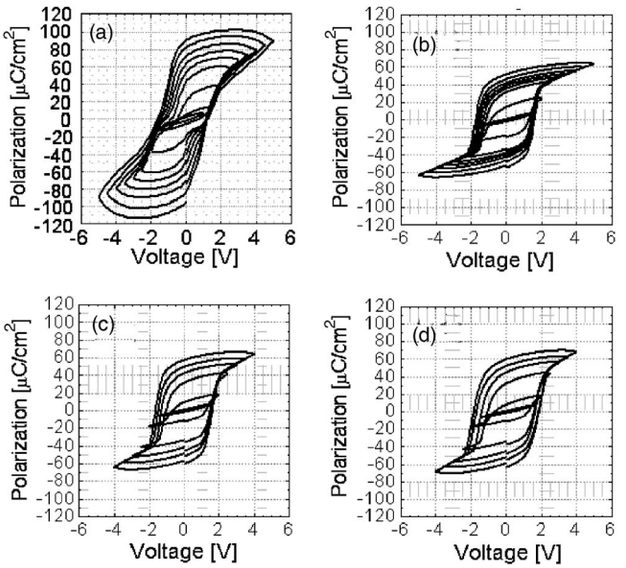

Figure 13. Ferroelectric hysteresis loop of a 70 nm thick PZT film on an (a) as-deposited and in O_2 in situ crystallized poly-SRO/type III substrate at (b) 550, (c) 600, and (d) 650°C.

oxidation state of Pb in the film grown on crystalline SRO is almost exclusively composed of Pb_3O_4. In addition to the variation in the binding status of Pb ions the Sr 3d signal also shows differences after the PZT deposition, depending on the crystallinity of SRO. As discussed in Fig. 6, the Sr state in amorphous SRO is less stable and vulnerable to chemical reactions with incoming Zr during the subsequent PZT deposition. The BE of the Sr 3d peak of amorphous SRO shifts into a lower energy direction after the PZT deposition. This might be due to the reaction with Zr, but the Sr 3d peak position of Sr–Zr–O compounds has not been reported. However, the peak location (~132.5 eV) is quite similar to that of crystalline $SrTiO_3$ (132.7 eV). Considering the similar chemical structure of Zr and Ti ions, it might be reasonable to assume that the peak shift in the lower BE direction is due to the formation of Sr–Zr–O compounds. This supports the previous hypothesis that Zr ions react with Sr and O on top of the amorphous SRO film during the initial stage of PZT MOCVD. It has to be noted that the molar standard formation energy of $SrZrO_3$ (−1514.717 kJ/mol) is lower than those of $SrTiO_3$ (−1419.698 kJ/mol) and $PbTiO_3$ (−941.332 kJ/mol) at 900 K.[27] This may constitute one of the reasons for the formation of Sr–Zr–O compounds during the initial stage of film growth on the relatively unstable SRO electrode. When the Sr–Zr–O phase is formed, the remaining Pb, Ti, Ru, and O may have a high chance to form Pb–Ti(Ru)–O and Pb–Ru–O compounds, which are believed to be electrically leaky. This may constitute one of the reasons for the high leakage current.

The location of Sr 3d in the in situ crystallized SRO is not notably changed after PZT deposition, as shown in Fig. 12b. Only the relative ratio of the two component peaks is changed, suggesting the better stability of this material compared to the amorphous SRO.

Growth and ferroelectric properties of PZT films on in situ poly-SRO electrodes.— As discussed previously, in situ crystallized poly-SRO films on type III substrates are quite stable in chemical and structural aspects compared to amorphous SRO or ex situ crystallized SRO electrodes. Therefore, it is expected that the PZT film deposited on an in situ crystallized SRO electrode produces good ferroelectric properties. Figure 13a shows the ferroelectric hysteresis loop of a 70 nm thick PZT film on in situ crystallized poly-SRO/type III substrate. It can be observed that ferroelectric hysteresis was obtained but the loop shapes are largely distorted, possibly due to the high leakage current and charge traps. This was assumed to be due to the still-unstable PZT/SRO interface. In order to improve the interface property, the in situ crystallized poly-SRO/type III substrate samples were heat-treated in two different oxidizing atmospheres before the PZT MOCVD: O_3 atmosphere (O_3 concentration of 250 g/m^3 with a total pressure of 1 Torr) at 300°C for 30, 100, and 300 s, respectively, and O_2 atmosphere at 1 atm using a furnace for 30 min at 550, 600, and 650°C, respectively. As will be shown later, the O_3 treatment was too harsh to the underlying Ru layer, so that the electrode stack became very rough by the oxidation of Ru, and thus, the PZT film grown on the O_3-treated substrates became very leaky and no P–V hysteresis loop was obtained. However, the furnace O_2 treatment was a proper method to improve the surface state of the in situ poly-SRO film as shown by the much better P–V loops shown in Fig. 13b-d, which correspond to the furnace O_2 treatments at 550, 600, and 650°C, respectively. The remanent polarization (P_r) of the PZT film on the furnace O_2-treated in situ poly-SRO electrode is as large as 35.5 μC/cm^2 at an applied voltage of 3 V. This is almost twice as large as that of the same film directly grown on an Ir electrode. This clearly shows the merit of adopting an SRO buffer layer in spite of the additional complexity of fabricating an optimized SRO film. However, the coercive voltage (~1.5 V) is quite high considering the relatively thin (~70 nm) thickness of the PZT film. The origin of this high coercive voltage is under investigation now.

However, the furnace O_2 treatments at higher temperature (>600°C) are not desirable compared to the same annealing at 550°C. The P–V loop shapes become leaky as the annealing temperature increases >600°C. The reasons for the large improvement in P–V performance by the furnace O_2 treatments at 550°C of the in situ poly-SRO film and degradation for the cases of the O_2 treatment at higher temperatures are investigated. The changes in the structures of the in situ poly-SRO/type III substrates by the O_3 treatments are also investigated. This was attempted to show the reason for the degradation by the O_3 treatment although O_3 is also a strong oxidant.

Figure 14a and b show the XRD patterns of a PZT film grown on an O_3-pretreated in situ poly-SRO/type III and furnace O_2-pretreated in situ poly-SRO/type III substrates, respectively. When the PZT film was grown on the nontreated in situ poly-SRO electrode, the XRD peaks corresponding to the PZT (100), (001), and (110), SRO(110), and Ru(002) planes are observed, suggesting that there was no substantial change in the stacked electrode structures. However, as the O_3-pretreatment time increases, the Ru(002) peak intensity largely decreases and finally becomes negligible after a treatment for 300 s. The SRO(110) peak intensity also decreases with increasing pretreatment time. It can be observed that a peak near 2Θ of 28° appears after a pretreatment for >100 s, which corresponds to the RuO_2(110) plane. Along with the changes in the crystalline structure in the electrode stack, the PZT peak intensity slightly decreases with increasing O_3 pretreatment time.

When the PDA condition was changed to furnace O_2 pretreatment, similar changes in the XRD patterns of the electrode stack are observed with increasing annealing temperature, but the degree of change is smaller than in the case of O_3 pretreatment. An appreciable Ru(002) peak intensity was still observed after annealing at 650°C. Accordingly, the degradation in the SRO and PZT peak intensities with increasing annealing temperature is less than that with increasing O_3-pretreatment time. These changes in the structures of the electrode layers are confirmed by the SEM observations shown in Fig. 15 and 16. Figure 15a-d shows the surface morphology of the as-deposited in situ poly-SRO/type III substrates and after O_3-pretreatment for 30, 100, and 300 s, respectively. The as-deposited in situ poly-SRO film surface is smooth (rms roughness of ~0.6 nm) and is comprised of uniform SRO grains with an average size of ~20 nm. Cross-sectional SEM shows that the electrode stack is composed of a ~40 nm thick poly-SRO layer and a ~25 nm thick Ru layer. The initial Ru thickness was 20 nm, suggesting that

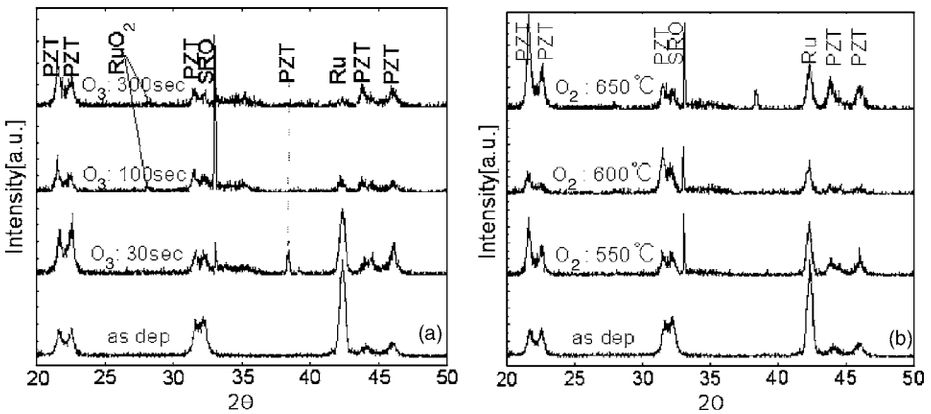

Figure 14. XRD patterns of a PZT film grown on (a) O_3-pretreated in situ poly-SRO/type III and (b) furnace O_2-pretreated in situ poly-SRO/type III substrates.

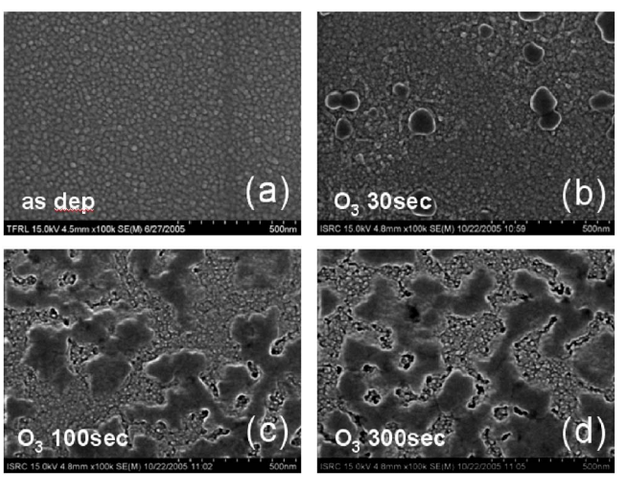

Figure 15. SEM surface morphology of (a) as-deposited in situ poly-SRO/type III substrates and after O_3 pretreatment for (b) 30, (c) 100, and (d) 300 s.

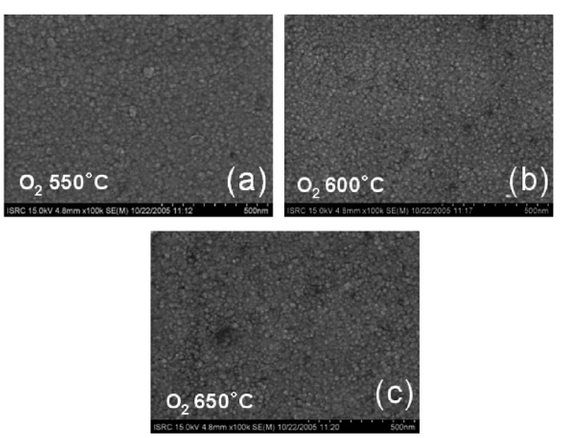

Figure 16. SEM surface morphology of in situ poly-SRO/type III substrates after furnace O_2 pretreatment at (a) 550, (b) 600, and (c) 650°C.

the SRO sputtering process at such a high T_g (550°C) already slightly oxidized the Ru layer. However, the O_3 pretreatment largely degrades the surface morphology of the electrode layer with the formation of a large irregular region. This irregular region might be the SrO-rich area, as is shown by the surface composition analysis using XPS. The underlying Ru layer becomes a bilayer structure with increasing O_3-pretreatment time. Considering the XRD data shown in Fig. 14a, this bilayer must be RuO_2/residual Ru, suggesting that the high oxidation potential of O_3 oxidized the underlying Ru layer in addition to inducing a chemical composition change in the SRO layer. It was noted that the total thickness of the bilayer does not increase with increasing O_3-pretreatment time, suggesting that some of the oxidized Ru evaporated during the O_3 pretreatment (39, 32, and 35 nm for 30, 100, and 300 s, respectively). It is believed that during the O_3 pretreatment Ru diffused into the SRO layer and formed volatile RuO_3 or RuO_4 along with nonvolatile RuO_2 by the reaction with the inward-diffused oxygen. This explains the changes in the XRD patterns shown in Fig. 14a, where the decrease in the Ru(110) peak intensity was not accompanied by an increase in the RuO_2(110) peak intensity. These degradations in the surface state of the poly-SRO electrode by O_3 pretreatment appear to be the origin of the failure of the ferroelectric performance of the PZT films grown on the O_3-pretreated SRO electrode.

Figure 16a-c shows the SEM surface morphology of the in situ poly-SRO/type III substrates after furnace O_2 pretreatment at 550, 600, and 650°C, respectively. The surface morphology does not show such a large change as in Fig. 15 but a slight increase in roughness (data shown later). However, the cross section shows a different modification with increasing furnace O_2-pretreatment temperature (data not shown). The poly-SRO thickness was almost invariant but the thickness of the underlying Ru layer increases from ~25 nm before the furnace O_2 pretreatment to ~45 nm after the furnace O_2 pretreatment at 650°C, without showing a distinctive bilayer structure. The XRD data shown in Fig. 14b did not show a large increase in the RuO_2 peak, suggesting that the increased underlayer is RuO_x ($x < 2$).

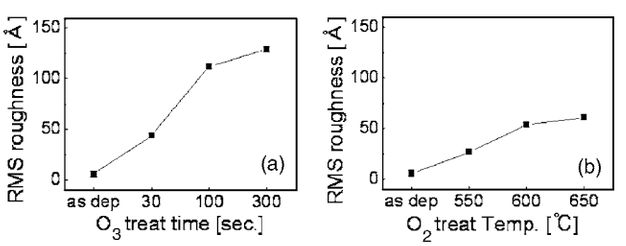

Figure 17. Variations in the rms surface roughness of in situ poly-SRO/type III substrates according to the (a) O_3 pretreatment and (b) furnace O_2 pretreatment conditions.

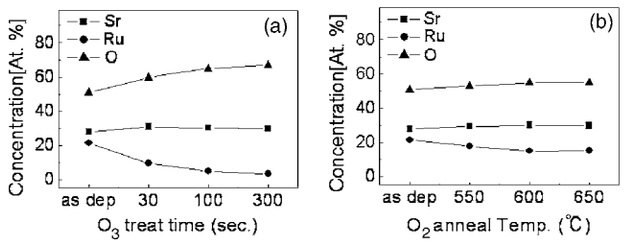

Figure 18. Changes in the surface chemical composition of a poly-SRO film monitored using XPS according to the (a) O_3 pretreatment and (b) furnace O_2 pretreatment conditions.

Figure 17a and b show the variations in the rms surface roughness of the in situ poly-SRO/type III substrates according to the O_3-pretreatment and furnace O_2-pretreatment conditions, respectively. The O_3 pretreatment largely increases the surface roughness in spite of the relatively low treatment temperature. The furnace O_2 pretreatment also increases the roughness, but the degree of increase is much less than that of the O_3 pretreatment.

The changes in the surface chemical composition of the poly-SRO film was monitored using XPS according to the O_3 pretreatment and furnace O_2 pretreatment conditions, and the results are shown in Fig. 18a and b, respectively. It can be understood that the pretreatments of the poly-SRO films in oxidizing atmosphere generally increase the O concentration and decrease the Ru concentration with a negligible change in Sr concentration. However, the degree of change is much more excessive for the case of O_3 pretreatments. The relative concentrations of each element shown in Fig. 18 are not accurate values because the XPS tool was not calibrated for quantification, so that only relative variations have relevance. Therefore, it can be understood that the usual oxygen diffusion by furnace O_2 pretreatments do not modify the electrode structure so largely, whereas the O_3 pretreatments largely degrade the electrodes.

The surface oxygen concentration increases with increasing furnace O_2-pretreatment temperature up to 600°C and then saturates. It can be assumed that the initial surface oxygen concentration of the as-deposited poly-SRO layer was lower than the equilibrium value due to the low oxygen partial pressure during the sputtering process. Therefore, the furnace O_2 pretreatment recovers the equilibrium oxygen concentration. From the saturation behavior of the oxygen concentration over the pretreatment temperature of 600°C, the oxygen concentration after the pretreatment at >600°C corresponds to the equilibrium value.

It has been reported that the work function of SRO depends on the oxygen concentration of the material.[28] The fully oxidized SRO has a work function of ~5.0 eV, whereas the oxygen deficient material has ~4.6 eV.[28] Although the work function of the electrode is not the sole factor that determines the interfacial potential barrier height, which is the major controlling factor for the leakage current,[29] a higher work function of the electrode generally produces a higher potential barrier at the ferroelectric/electrode interface.[30-32]

Therefore, the better ferroelectric P–V performance of the PZT film on the furnace O_2-pretreated poly-SRO electrode shown in Fig. 13b must be due to an improved interfacial potential barrier at the PZT/SRO interface. If the work function was the sole factor that determines the leakage current, the P–V performance of the PZT film on the furnace O_2-pretreated poly-SRO electrode at 600 and 650°C should have been better. This suggests that the surface roughness also influences the leakage and P–V behavior.

Figure 19 shows the SEM surface morphology of 70 nm thick PZT films grown on O_3-pretreated and furnace O_2-pretreated poly-SRO electrodes under the various conditions. It is interesting to note that the surface morphology of the PZT films grown on the various SRO electrodes is not so different in spite of the largely different electrical measurement results. This shows the large influence of the PZT/electrode interface states on the electrical performances of the thin (<100 nm) ferroelectric PZT films.

Conclusion

Structural and electrical properties of in situ and ex situ crystallized polycrystalline SRO thin-film electrodes fabricated by dc magnetron sputtering at a substrate temperature of 550 and 350°C, respectively, followed by postannealing for application as bottom electrodes of MOCVD PZT thin films are investigated. The in situ crystallized SRO electrode shows a negligible change in the film composition during the subsequent annealing and works as a good electrode for the ferroelectric PZT films. However, the ex situ crystallization by post annealing of the amorphous as-deposited SRO film largely decreases the Ru content in the SRO film, and consequently the PZT film grown on top has a poor ferroelectric performance. In addition, the Zr component in the PZT film initially reacts with the excessive SrO in the electrode, resulting in a deposition of $PbTiO_3$ at the initial stage of PZT deposition. The structurally and chemically unstable properties of amorphous and ex situ crystallized SRO electrodes largely degrade the ferroelectric performance of the PZT thin films. The better structural and chemical stability of the in situ crystallized poly-SRO results in a reasonable ferroelectric performance of the PZT films. However, the oxygen-deficient surface composition of the as-deposited in situ poly-SRO electrode is the origin of an unsatisfactory ferroelectric performance. The pretreatment of the in situ poly-SRO electrode in O_2 atmosphere using a furnace at temperatures ranging from 550 to 600°C recovers the oxygen stoichiometric composition of the SRO layer, which results

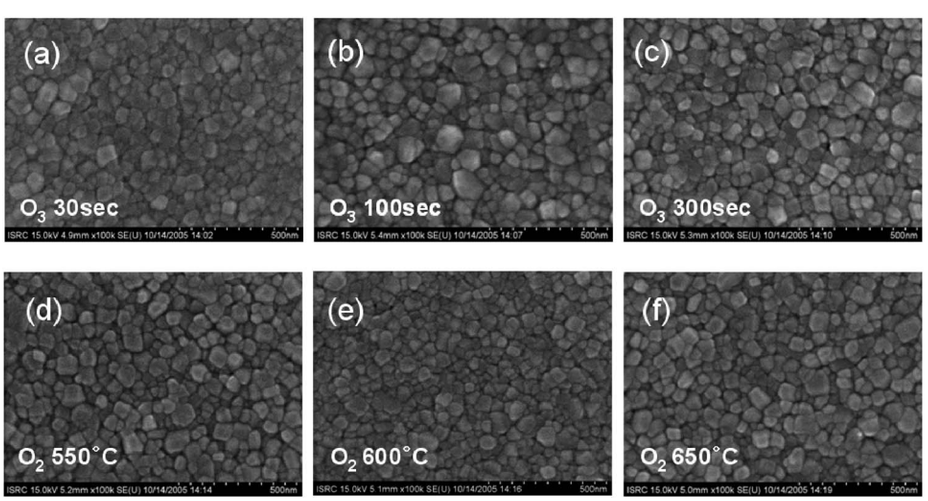

Figure 19. SEM surface morphology of 70 nm thick PZT films grown on (a–c) O_3-pretreated and (d–f) furnace O_2-pretreated poly-SRO electrodes under various conditions.

in a large improvement in the ferroelectric performance of the PZT film. The 70 nm thick PZT film grown on this properly pretreated in situ poly-SRO electrode shows a saturation P_r of 35.5 $\mu C/cm^2$ at an applied voltage of 3 V. However, too much oxidation of the SRO electrode using O_3 treatment was very harmful to the electrical property.

Seoul National University assisted in meeting the publication costs of this article.

References

1. J. F. Scott and C. A. Paz de Araujo, *Science*, **246**, 1400 (1989).
2. Y. Horri, Y. Hikosaka, A. Itoh, K. Matsuura, M. Kurasawa, G. I. Komuro, K. Maruyama, T. Eshita, and S. Kashiwagi, *Tech. Dig. - Int. Electron Devices Meet.*, **2002**, 539.
3. T. Nakamura, Y. Nakao, A. Kamisawa, and H. Takasu, *Appl. Phys. Lett.*, **65**, 1522 (1994).
4. J. E. Heo, B. J. Bae, D. C. Yoo, S. D. Nam, J. E. Lim, D. H. Im, S. O. Park, H. S. Kim, U. I. Chung, and J. T. Moon, Extended Abstracts of the 2005 SSDM, p. 1028–1029, Kobe, Japan, Sept 12-15 (2005).
5. C. B. Eom, R. B. Van Dover, Julia M. Phillips, D. J. Werder, J. H. Marshall, C. H. Chen, R. J. Cava, R. M. Fleming, and D. K. Fork, *Appl. Phys. Lett.*, **63**, 2570 (1993).
6. V. Nagarajan, S. Prasertchoung, T. Zhao, H. Zheng, J. Ouyang, R. Ramesh, W. Tian, X. Q. Pan, D. M. Kim, C. B. Eom, H. Kohlstedt, and R. Waser, *Appl. Phys. Lett.*, **84**, 5225 (2004).
7. C. B. Eom, R. J. Cava, R. M. Fleming, J. M. Phillips, R. B. van Dover, J. H. Marshall, J. W. P. Hsu, J. J. Krajeuski, and W. F. Peck, Jr., *Science*, **258**, 1766 (1993).
8. S. Aggarwal, I. G. Jenkins, B. Nagaraj, C. J. Kerr, C. Canedy, R. Ramesh, G. Velasquez, L. Boyer, and J. T. Evans, Jr., *Appl. Phys. Lett.*, **75**, 1787 (1999).
9. K. Aoki, I. Murayama, Y. Fukuda, and A. Nishimura, *Jpn. J. Appl. Phys., Part 2*, **36**, L690 (1997).
10. J. S. Cross, M. Fujiki, M. Tsukada, Y. Kotaka, and Y. Goto, *Integr. Ferroelectr.*, **21**, 263 (1998).
11. Y. K. Kim, H. Morioka, R. Ueno, S. Yokoyama, and H. Funakubo, *Appl. Phys. Lett.*, **86**, 212905 (2005); N. Okuda, K. Saito, and H. Funakubo, *Jpn. J. Appl. Phys., Part 1*, **39**, 572 (2000); H. Funakubo, T. Oikawa, N. Higashi, and K. Saito, *J. Cryst. Growth*, **235**, 401 (2002); N. Higashi, T. Watanabe, K. Saito, I. Yamaji, T. Akai, and H. Funakubo, *J. Cryst. Growth*, **229**, 450 (2001).
12. S. Y. Kang, C. S. Hwang, and H. J. Kim, *J. Electrochem. Soc.*, **152**, C15 (2005).
13. J. S. Zhao, D. Y. Park, M. J. Seo, and C. S. Hwang, *J. Electrochem. Soc.*, **151**, C283 (2004).
14. J. M. Koo, B. S. Seo, S. P. Kim, S. M. Shin, J. H. Lee, H. S. Baik, J. H. Lee, J. H. Lee, B. J. Bae, J. E. Lim, D. C. Yoo, S. O. Park, H. S. Kim, H. Han, S. G. Baik, J. Y. Choi, Y. J. Park, and Y. S. Park, *Tech. Dig. - Int. Electron Devices Meet.*, **2005**, 539.
15. A. Nagai, H. Morioka, G. Asano, H. Funakubo, and A. Saiki, *Appl. Phys. Lett.*, **86**, 142906 (2005).
16. H. Fujisawa, S. Watari, N. Iwamoto, M. Shimizu, H. Niu, and N. Oshima, *Integr. Ferroelectr.*, **68**, 85 (2004).
17. Y. Noro and S. Miyahara, *J. Phys. Soc. Jpn.*, **27**, 518 (1969).
18. J. A. Rard, *Chem. Rev. (Washington, D.C.)*, **85**, 1 (1985).
19. J. F. Moulder, W. F. Stickle, P. E. Sobol, and K. D. Bomben, *Handbook of X-Ray Photoelectron Spectroscopy*, p. 104–105, Perkin-Elmer Corp., Eden Prairie, MN (1992).
20. H. Funakubo, G. Asano, T. Ozeki, H. Machida, T. Yoneyana, and Y. Takamatsu, *J. Electrochem. Soc.*, **151**, C463 (2004).
21. G. J. Mormans, P. J. wan Veldhoven, and M. De Keijser, *J. Cryst. Growth*, **123**, 537 (1992).
22. J. S. Zhao, H. J. Lee, J. S. Sim, K. Lee, and Cheol Seong Hwang, *J. Electrochem. Soc.*, **153**, F81 (2006).
23. J. F. Moulder, W. F. Stickle, P. E. Sobol, K. D. Bomben, *Handbook of X-Ray Photoelectron Spectroscopy*, p. 108–109, Perkin-Elmer Corp., Eden Prairie, MN (1992).
24. A. Nagai, H. Morioka, G. Asano, and H. Funakubo, *Appl. Phys. Lett.*, **82**, 23 (2003).
25. C. S. Hwang and H. J. Kim, *J. Am. Ceram. Soc.*, **78**, 329 (1995).
26. J. F. Moulder, W. F. Stickle, P. E. Sobol, K. D. Bomben, *Handbook of X-Ray Photoelectron Spectroscopy*, p. 188–189, Perkin-Elmer Corp., Eden Prairie, MN (1992).
27. I. Barin, *Thermochemical Data of Pure Substances, Part II*, p. 1157,1433, and 1436, VCH, Weinheim (1989).
28. A. J. Hartmann, M. Neilson, R. N. Lamb, K. Watanabe, and J. F. Scott, *Appl. Phys. A*, Vol. **A70**, 239 (2000).
29. A. M. Cowley and S. M. Sze, *J. Appl. Phys.*, **36**, 3212 (1965).
30. J. D. Baniecki, T. Shioga, K. Kurihara, and N. Kamehara, *J. Appl. Phys.*, **94**, 6741 (2003).
31. J. C. Shin, C. S. Hwang, H. J. Kim, and S. O. Park, *Appl. Phys. Lett.*, **75**, 3411 (1999).
32. J. F. Scott, *Ferroelectric Memories*, p. 116, Springer, New York (2000).